# LIMNOLOGY and OCEANOGRAPHY: METHODS



Limnol. Oceanogr.: Methods 20, 2022, 618–632
© 2022 The Authors. Limnology and Oceanography: Methods published by
Wiley Periodicals LLC on behalf of Association for the Sciences of
Limnology and Oceanography.
doi: 10.1002/lom3.10509

# A novel method to study the fragmentation behavior of marine snow aggregates in controlled shear flow

Yixuan Song <sup>0</sup>, <sup>1</sup> Matthew J. Rau <sup>0</sup><sup>2</sup>\*

<sup>1</sup>Department of Mechanical Engineering, The Pennsylvania State University, University Park, Pennsylvania

#### **Abstract**

The sinking of marine aggregates impacts the global carbon cycle as it is one of the primary sources of carbon export from the surface ocean. Aggregation and fragmentation alter the size of aggregates, which governs their sinking speed. Although aggregation theory is well established, aggregate fragmentation strength and breakup characteristics are less well understood. This study developed a cylindrical tank that formed and then exposed diatom aggregates to calibrated laminar shear through a combined rotating and oscillating motion. The shear rate was predictable using a developed analytical solution for the fluid motion within the tank. Under proper operating conditions, this facility provided fluid shear with a similar magnitude to that in multiple ocean environments. We also developed a unique image processing method that enabled continuous tracking of particles' position, size, and morphology as well as determination of the individual aggregate breakup events. The method has great potential to capture breakup events of large marine snow particles, quantify the aggregate morphological changes leading up to and at breakup, and provide data sufficient for statistical analysis of laboratory aggregate populations. We tested the method using laboratory-cultured *Odontella aurita* and captured 79 breakup events of the resulting aggregates. These fragmented aggregates ranged from 1 to 5 mm in major axis length and underwent substantial morphological evolutions prior to the fragmentation.

Aggregated particulate organic matter in the ocean, known as marine snow, makes up a large part of the oceanic sedimentary flux and is key to biological transformations in marine ecosystems (Kiørboe 2001). In shallow waters, up to 63% of the particulate organic carbon can be contained within marine snow, the size of which can range from a few microns up to centimeters (Alldredge and Silver 1988). Every year, approximately 10<sup>15</sup> g of carbon is pumped from the surface ocean to the deep sea by sinking marine snow particles (Muller-Karger 2005; Middelburg 2011). In the natural environment, the settling velocity of marine snow varies widely (Cael et al. 2021) but has been observed to be as high as 0.43 cm s<sup>-1</sup>

\*Correspondence: matthew.rau@gwu.edu

Additional Supporting Information may be found in the online version of this article.

This is an open access article under the terms of the Creative Commons Attribution-NonCommercial-NoDerivs License, which permits use and distribution in any medium, provided the original work is properly cited, the use is non-commercial and no modifications or adaptations are made.

**Author Contribution Statement:** Y.S. designed and performed the experiments and analyzed the data. M.J.R. was involved in planning and supervising the work. Y.S. and M.R. assessed the methods and drafted the manuscript.

(370 m d<sup>-1</sup>) (Alldredge and Gotschalk 1988). These sinking particles are the primary source of carbon fixation in the ocean and this process significantly affects the concentration of CO<sub>2</sub> in the atmosphere (Kwon et al. 2009). Carbon flux measurements have revealed an exponential decrease in this downward flux of organic materials with depth (Berger 1988), which has not yet been fully explained. Degradation of sinking particles caused by attached bacteria and the consumption by zooplankton are major sources of this decrease, but these processes alone do not fully explain the attenuation observed in the environment (Collins et al. 2015). Fragmentation of large sinking aggregates into slower-settling sub-aggregates is one likely explanation that could reconcile the carbon budget (Briggs et al. 2020). While aggregation theory has been well developed (Fowler and Knauer 1986; Alldredge and Silver 1988; Burd and Jackson 2009) and its influence on particle flux is represented in ocean transport models (Aumont et al. 2015), fragmentation processes have not yet reached this same level of parametric understanding.

Small scale fluid shear in the ocean, characterized by dissipation energy, causes aggregation, fragmentation, and aggregate morphological changes. These processes determine particle size, which in turn governs settling velocity (Johnson et al. 1996). Fragmentation of large aggregates due to this fluid

<sup>&</sup>lt;sup>2</sup>Department of Mechanical and Aerospace Engineering, The George Washington University, Washington, District of Columbia

shear is challenging to investigate. Traditionally, researchers first form laboratory-made marine aggregates using cylindrical roller tanks, which aggregate particles through differential sedimentation (Shanks and Edmondson 1989). They are then transferred to separate shear- or turbulence-generating facilities to study the fragmentation process (Alldredge et al. 1990; Saha et al. 2016; Ziervogel et al. 2020). In order to imitate the ocean environment, Alldredge et al. (1990) quantified the breakup strength of collected natural marine snow using turbulence generated with an oscillating grid. Here, aggregates were collected, stored briefly, and then released individually into their turbulence tank. Ziervogel et al. (2020) similarly studied fragmentation of marine oil snow by first creating laboratory-made aggregates in a roller tank and then manually transferring the aggregates to a turbulence tank to observe fragmentation at different levels of turbulence intensities. Fuchs et al. (2004) used a similar grid-stirred tank to observe the sinking behaviors of marine gastropod larvae where they had to gently add samples into the tank before measuring larval movement. In addition to requiring manipulation of the particles by the researchers prior to measurement, the above cases also quantified shear rates using time-average values of energy dissipation rate. Measuring the instantaneous local shear forces acting on the particles was not possible. Goldthwait et al. (2004) analyzed the fragmentation of marine snow due to swimming euphausiids. To obtain local timeaveraged fluid stresses caused by the feeding animals, they performed separate particle image velocimetry experiments using tethered animals, then assumed the shear magnitude was unchanged during animal interaction with an aggregate. In these works, researchers could not couple the time-varying responses of aggregates to local instantaneous hydrodynamic phenomena due to their time-averaged characterization.

In more detailed experiments, previous researchers have used various flow devices to resolve hydrodynamic conditions to study the local fragmentation of droplets and other types of particle aggregates. For example, laboratory observations captured droplet deformation, and breakage in simple shear flows generated by a Couette device (Torza et al. 1972; Williams et al. 1997). With flow conditions determined analytically, the researchers could determine transient shapes and droplet bursting and their dependence on instantaneous hydrodynamics. Saha et al. (2014, 2016) investigated the breakup of colloidal aggregates in an extensional flow using contracting nozzles and in-homogenous isotropic turbulence with threedimensional particle tracking velocimetry (3D-PTV) techniques. They measured velocity gradients to determine the local fluid stress at the instant of individual aggregate breakup. The spatially and temporally resolved data from the above experiments have provided unique insights into the morphological evolution of droplets and aggregates exposed to hydrodynamic shear. The need exists for a facility that enables high numbers of detailed fragmentation measurements like those described above to clarify the fragmentation dynamics of marine aggregates. Due to their fragile nature, avoiding aggregate manipulation after formation is also desirable as handling can alter their morphology and strength.

This article introduces a novel roller tank that can aggregate and fragment marine snow particles by combining constant rotation with an oscillatory motion. The tank avoids all handling of the marine snow by experimentalists. More importantly, when coupled to high-speed imaging and automated particle tracking and matching algorithms, this experimental approach allows us to quantify the instantaneous responses of marine snow to hydrodynamic shear while also evaluating large statistical samples (e.g., 100,000 s particles). To demonstrate its effectiveness and capabilities, we present breakup experiments of marine snow made from Odontella aurita. We organize the paper with the following sections. In the "Materials and procedures" section, we describe the design of the rotating/oscillating tank and formulate the analytical solution to fluid shear inside this tank. We also demonstrate the image processing procedures for continuously tracking marine aggregates and identifying breakage. In the "Assessment" section, we present the fragmentation results with their morphological evolutions using both individual and statistical analyses. In addition, we discuss the significance of morphological changes prior to fragmentation and quantify aggregate strengths. In the "Discussion" section, we discuss the limitations of the method and evaluate the overall performance. Finally, in the "Comments and recommendations" section, we make concluding marks and address recommendations for future work.

# Materials and procedures

# **Experimental facility**

The experimental facility, shown in Fig. 1, consisted of a transparent acrylic cylindrical tank supported by four identical casters. The tank had an inner diameter of 100 mm and a wall thickness of 5 mm with a total length of 300 mm. The tank was long enough to have a two-dimensional (2D) flow along the central tank cross-section (Song and Rau 2020a). We controlled the rotation of this tank using an electric servo-motor (Dynamixel MX-28T, Trossen Robotics) programmed with Python. A timing belt drive system that connected the motor to one end of the tank precisely synchronized the rotation with a gear ratio of one. The motor had a resolution of  $0.012 \text{ rad s}^{-1}$  in rotation speed and  $0.088^{\circ}$  in operating angle. The optical transparency of the tank permitted illumination through the cylinder wall and the imaging of suspended particles through one end of the tank. An LED light panel (StudioPRO S-1200D, Fovitec) shone through a slit aperture (10 mm wide) to illuminate suspended particles along the central tank cross-section. We mounted a high-speed camera (FASTCAM Mini AX200, Photron) with its viewing axis perpendicular to the resulting light sheet. It captured particle motion through a macro lens with a 105 mm focal length (Sigma 105 mm f/2.8 EX DG).

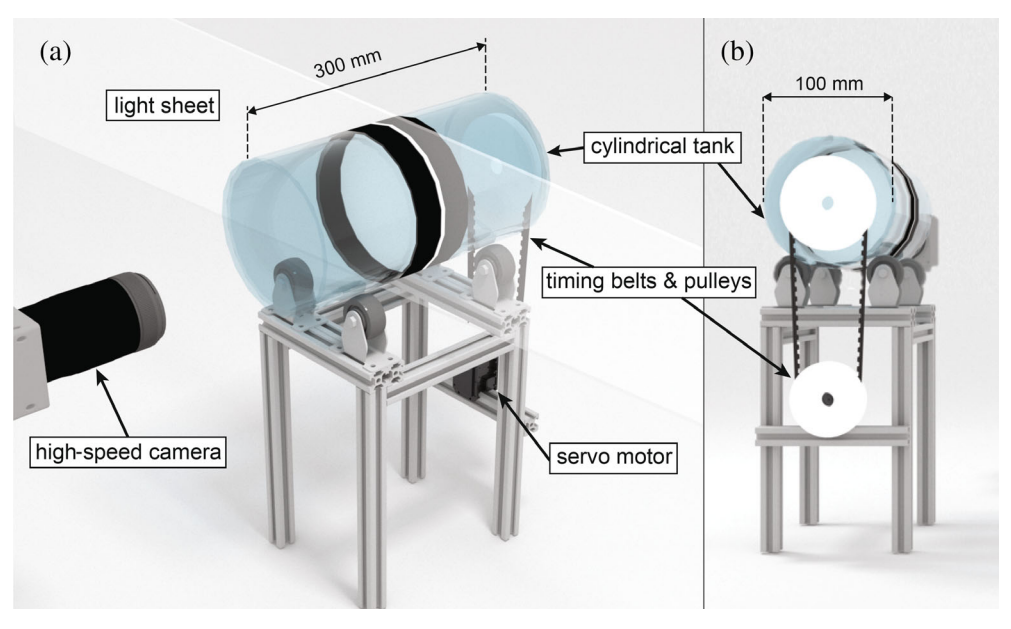
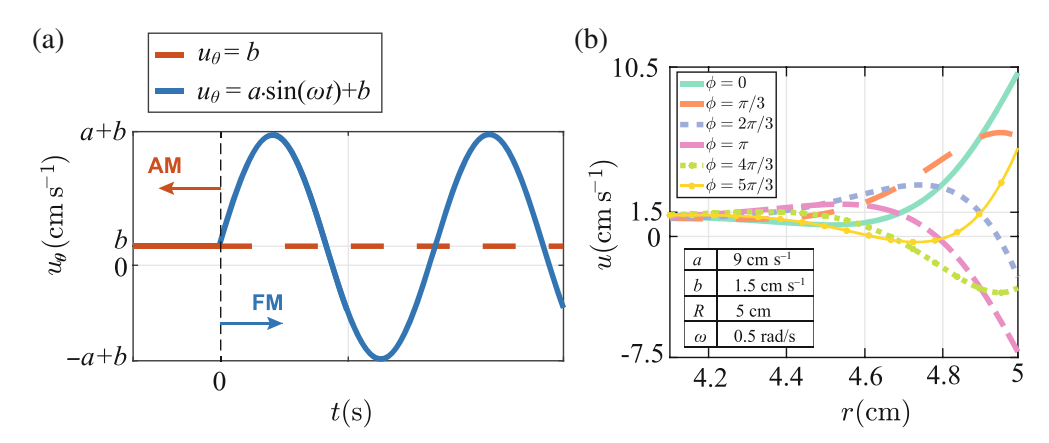


Fig. 1. Schematic diagram of the experimental facility.

The servo motor allowed us to vary and control the tank rotation speed. The roller tank was in its aggregation mode (AM) when we operated the tank at a constant rotation rate. We found that the phytoplankton aggregated quickly in AM and formed large, stable aggregates through differential sedimentation after about 3 h of operation. This aggregation time is similar to the aggregation time used in prior work (Shanks and Edmondson 1989) and all of our fragmentation experiments started with 3 h of AM operation. Once diatom aggregates were formed, we initiated the fragmentation mode (FM) by superimposing a harmonic oscillation to the tank rotation. This continuously varied the speed of the outer tank wall, as shown in Fig. 2a, which caused an oscillating laminar boundary layer to form around the tank circumference (Song and Rau 2020a). The rotation

and oscillation created time-varying fluid shear due to a velocity gradient that extended inwards toward the center of the tank. This dynamic creation of velocity gradients in the tank allowed us to directly expose aggregates to hydrodynamic shear without handling or moving them to a second facility.

We previously developed an analytical solution to describe the fluid motion in a similar tank with a symmetric oscillation (Song and Rau 2020a). Particle image velocimetry (PIV) experiments confirmed the validity of the analytical results and that the flow along the central tank cross-section remained 2D and laminar. Here, we modified this analytical solution to include the oscillating motion plus the constant rotation of the roller tank. Assuming the saltwater is an incompressible Newtonian fluid with a constant kinematic viscosity  $\nu$ , we can simplify



**Fig. 2.** (a) Sample wall boundary conditions for both aggregation mode and fragmentation mode, and (b) one period of quasi-steady velocity profiles plotted at different phase angles during fragmentation mode.

the 3D Navier Stokes equation to contain only the azimuthal component, as shown in Eq. 1,

$$\frac{\partial u_{\theta}}{\partial t} = \nu \left( \frac{1}{r} \frac{\partial u_{\theta}}{\partial r} + \frac{\partial^2 u_{\theta}}{\partial r^2} - \frac{u_{\theta}}{r^2} \right). \tag{1}$$

In Eq. 1, gravity is neglected as it integrates to zero in the azimuthal direction assuming no free surfaces are present inside of the closed cylinder. During the switch from AM to FM, the fluid experiences a change in the outer wall boundary condition. Shown in Fig. 2a as a constant rotation speed  $u_{\theta} = b$  in AM, this boundary condition changes to  $u_{\theta} = a\sin(\omega t) + b$  in FM, where a is the amplitude and  $\omega$  the angular frequency of the superimposed harmonic oscillation. In our analysis, we assume the tank has rotated in AM for a long enough time that the fluid velocity is a steady solid-body rotation. The resulting initial and boundary conditions representing a sudden change from AM to FM are thus,

$$u_{\theta}(r,0) = \frac{r}{R}b,\tag{2a}$$

$$u_{\theta}(R, t) = a \cdot \sin(\omega t) + b,$$
 (2b)

$$u_{\theta}(0,t) = 0. \tag{2c}$$

where *R* is the inside radius of the tank. The resulting transient solution, which contains the transition motion from solid body rotation, is written as,

$$\begin{split} u_{\theta}(r,t) &= \frac{r}{R}b + \frac{a}{2} \left[ exp \left( i\omega t - i\frac{\pi}{2} \right) \frac{I_{1} \left( r\sqrt{i\omega/\nu} \right)}{I_{1} \left( R\sqrt{i\omega/\nu} \right)} \right. \\ &+ exp \left( -i\omega t + i\frac{\pi}{2} \right) \frac{I_{1} \left( r\sqrt{-i\omega/\nu} \right)}{I_{1} \left( R\sqrt{-i\omega/\nu} \right)} \right] \\ &+ a \cdot \sum_{n}^{\infty} exp \left( z_{0,n} \omega t \right) \frac{4z_{0,n}^{1/2}}{\left( z_{0,n}^{2} + 1 \right) R\sqrt{\omega/\nu}} \\ &\cdot \frac{I_{1} \left( r\sqrt{z_{0,n} \omega/\nu} \right)}{I_{0} \left( R\sqrt{z_{0,n} \omega/\nu} \right) + I_{2} \left( R\sqrt{z_{0,n} \omega/\nu} \right)}, \end{split}$$

where  $I_0$ ,  $I_1$ , and  $I_2$  are the modified Bessel functions of the first kind and order zero, one, and two, respectively. The variable  $z_{0,n}$  is defined as,

$$z_{0,n} = -\frac{\alpha_n^2 \nu^2}{R^2 \omega^2},\tag{4}$$

where  $\alpha_n$  is the  $n^{\text{th}}$  zero of  $J_1$ , the Bessel function of the first kind and order one. The details of the mathematical solution procedure to derive Eq. 3 are identical to those provided by Song and Rau (2020*a*) and have, thus, been omitted here for

brevity. Equation 3 consists of three terms: the first term represents solid body rotation, the second term represents the oscillating velocity at different radial locations, and the third term represents a rapidly decaying transient motion due to the transition between AM and FM. This third transient term decays within one cycle of oscillation (Song and Rau 2020a), after which we can neglect the transient term in Eq. 3 and assume the fluid motion inside the tank obtains a periodic state represented by,

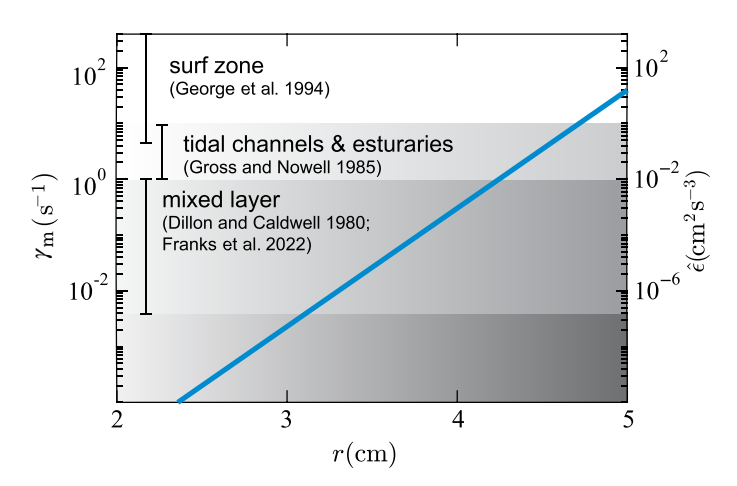
$$u_{\theta,s}(r,t) = \frac{r}{R}b + \frac{a}{2} \left[ \exp\left(i\omega t - i\frac{\pi}{2}\right) \frac{I_1\left(r\sqrt{i\omega/\nu}\right)}{I_1\left(R\sqrt{i\omega/\nu}\right)} + \exp\left(-i\omega t + i\frac{\pi}{2}\right) \frac{I_1\left(r\sqrt{-i\omega/\nu}\right)}{I_1\left(R\sqrt{-i\omega/\nu}\right)} \right].$$
 (5)

Figure 2b shows periodic velocity profiles at six different phase angles within one period of oscillation during FM for an oscillation magnitude of a = 9 cm s<sup>-1</sup> and the constant rotation rate b = 1.5 cm s<sup>-1</sup> for a tank with an inner radius of R = 5 cm (this constant rotation rate is equivalent to a rotation speed of 2.86 rpm). The velocity variation is maximum close to the outer wall of the tank, which is reflected in the boundary layer thickness  $\delta = \sqrt{\nu/\omega}$  (Song and Rau 2020a). However, we will show below how the small velocity variation further from the tank wall still creates shear of relevance to the ocean and aggregate fragmentation outside of the boundary layer does occur. We can use Eq. 5 to calculate the azimuthal velocity as a function of radius inside any oscillating roller tank so long as the appropriate speed and dimensional parameters are adjusted in the equation (i.e., a, b, R, and  $\omega$ ) and the tank maintains a laminar, 2D flow. We validated these latter two conditions experimentally and found the equation valid for dimensionless radii  $\sqrt{\omega R^2/\nu}$  in excess of 35.7 (Song and Rau 2020a), though the upper limit of validity was not determined. The operating conditions in this work correspond to a dimensionless radius of 34.3, though many different operating conditions could be used with this method to tune the shear conditions in the tank to a particular application of interest.

Knowing the fluid velocity from Eqs. 3 and 5, we can calculate the time-varying laminar shear,  $\gamma$ , during FM as,

$$\gamma = r \frac{\partial (u_{\theta}/r)}{\partial r}.$$
 (6)

As a result of the oscillating velocity profiles, the shear rate oscillates with small amplitudes near the tank center and large amplitudes near the tank wall. Figure 3 shows the maximum shear rate,  $\gamma_{\rm m}$ , as a function of radius for the velocities plotted in Fig. 2b. Also plotted are equivalent dissipation rates,  $\hat{\epsilon}$  calculated from  $\gamma = \sqrt{\hat{\epsilon}/\nu}$ . We can compare shear in the tank to that



**Fig. 3.** Theoretical maximum shear in the tank compared to typical shear observed in the ocean.

generated in typical ocean conditions based on the ranges given by Dillon and Caldwell (1980) and Franks et al. (2022) for mixed-layer turbulence, Gross and Nowell (1985) for tidal channels and estuaries, and George et al. (1994) for surf zones. Using the prescribed conditions, the regions close to the tank wall provide high shear rates typical of the most turbulent regions of the ocean, whereas the inner regions provide shear more typical of the open ocean. We can adjust the range of shear in the tank by modifying the tank dimensions or oscillation magnitude or frequency as indicated in Eq. 5.

To perform an experiment, we first filled the cylindrical tank with cultured algae at a concentration of approximately 46,000 cells mL<sup>-1</sup> and filtered seawater (Gulf of Maine Seawater, Bigelow NCMA, 30 parts per thousand [ppt] salinity), being careful to fill the tank fully so that no air was trapped after the tank end cap was secured. We could use other concentrations, but we found this level to be a good compromise between having enough algae to quickly form large aggregates while also not too many to prevent good optical access within the tank. The low concentrations and relatively small excess density of the particles also ensured that the bulk flow of the tank was not modified by the particle suspension. We then aggregated particles in AM for 3 h. After we formed aggregates, the roller tank oscillated in FM while we recorded images with the high-speed camera until its memory was full.

#### **Imaging methods**

Example color pictures of the experiment taken with a digital camera are shown in Fig. 4. The phytoplankton prior to aggregation are shown in Fig. 4a, with Fig. 4b,c showing the resulting aggregates after 3 h of AM operation, and after 174.7 s of FM operation, respectively. To resolve time-varying morphological changes and breakup, we utilized a high-speed camera and bright illumination for the actual aggregate tracking experiments. We illuminated aggregates using the LED light panel and a slit aperture as described above.

The camera focused on illuminated aggregates through one end of the cylindrical tank. Figure 4e,f shows the resulting gray-scale images of the aggregates in AM and FM, respectively. To calibrate the camera magnification as it viewed through the polycarbonate and seawater, we 3D printed a circular calibration plate to as shown in Fig. 4d. The plate had a diameter of 100 mm, with 8 mm horizontal and vertical spacings between adjacent dots. This calibration plate had a high finishing level with a tolerance of 0.002 in. (0.05 mm). Magnification varied from 10.28 px mm $^{-1}$  at the back of the light sheet to 10.40 px mm $^{-1}$  at the front, which gave us a mid-sheet magnification of 10.34 px mm $^{-1}$  with an uncertainty of  $\pm$  0.57%. We used this magnification for all subsequent calculations.

We recorded image frames at a rate of 125 fps with a shutter speed of  $1/1000~\text{s}^{-1}$ . For each experiment, we recorded 21,841 image frames, equivalent to 174.7 s. The high-speed camera started recording simultaneously with the change in tank motion from AM to FM and was controlled using an Arduino Uno board. We estimated that the delay between the camera trigger signal and the actual change in the motion of the varying-speed motor was  $5.5 \pm 2.5$  ms. The signal delay resulted in uncertainty in determining the phase angle corresponding to each image of up to  $8.36 \times 10^{-4}~\text{rad}$ .

#### Imaging processing procedures

#### Background removal

Time-dependent light reflections caused a nonuniform background in our experimental images, as shown in Fig. 5a, which complicated the particle identification and matching. Before particle identification, we removed the background of the gray-scale images using the proper orthogonal decomposition (POD) method initially developed by Mendez et al. (2017) for particle image velocimetry. One complication occurred for particles with slight motion inside the tank, which could be mistakenly considered part of the background due to their very small displacement. To avoid this, we used every 100<sup>th</sup> image in each series for the POD analysis, which exaggerated the motion of the particles for more consistent background detection.

# Particle identification

Capturing the 2D morphology of marine aggregates is challenging given that they can deform and have fractal features that influence their illumination, as shown in Fig. 5a,b. We developed a practical binarization approach to deal with the nonuniform background and blurry aggregate boundaries to get around these issues. This method applied a locally adaptive black-and-white threshold to obtain the morphology of individual particles. First, we segmented the gray image into smaller sub-images, as shown in Fig. 5b, and eliminated out-of-focus particles based on their grayscale intensities. Next, we calculated the grayscale intensity gradients shown in Fig. 5c and applied the local adaptive binarization (Fig. 5d). After a dilation-and-erosion step (Fig. 5e), we captured the shape of every particle remaining in the image. Finally, we masked all

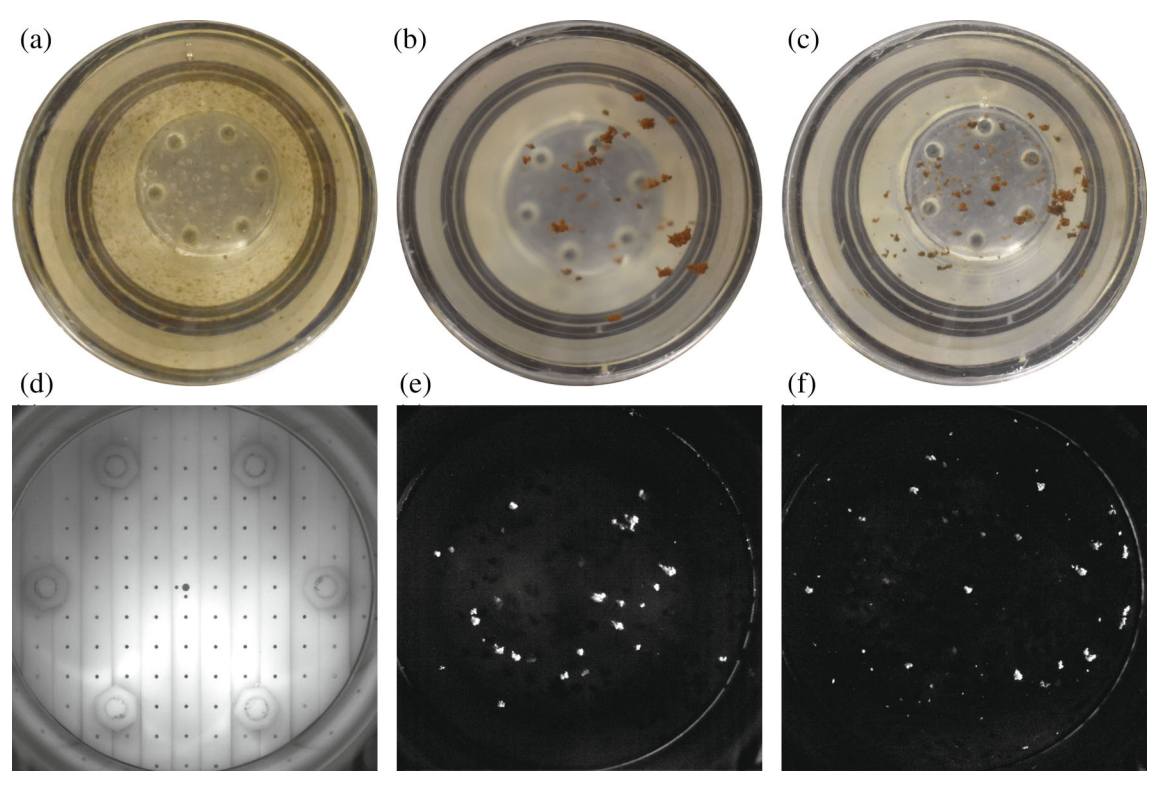


**Fig. 4.** Pictures of the phytoplankton (**a**) prior to aggregation, (**b**) after 3 h of aggregation in AM, and (**c**) after 174.7 s in FM. The circular calibration plate used to determine magnification is shown in (**d**). High-speed images used for analysis are shown in (**e**) for aggregates in AM and (**f**) aggregates after fragmentation in FM.

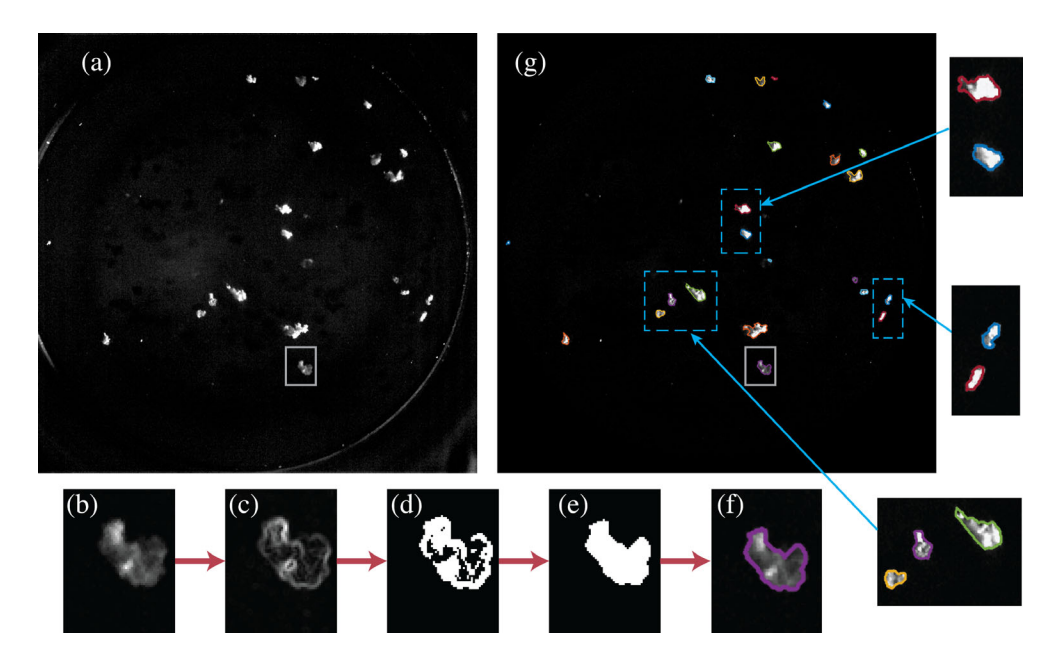


**Fig. 5.** Grayscale images of aggregates (**a**) before applying a static mask and background removal, (**b–f**) major steps for binarization and edge detection, and (**g**) after the particle identification. The image in (**g**) shows the same aggregates as those in (**a**). Samples of particles with their exterior boundaries after the identification are provided next to (**g**).

individual gray images of particles (Fig. 5f) for the subsequent particle matching process. An example final image is shown in Fig. 5g with a few zoomed-in particle images next to it. Further details of these image processing steps are provided in Supporting Information S1.

#### Particle matching

We developed an aggregate matching algorithm to track morphological changes and breakup events of individual aggregates over time. Before the matching began, we assigned each aggregate in the first frame of the image time series a unique identifying number. Then the algorithm searched for matches to each of these aggregates in the subsequent frames, as described below. Individual aggregates were tracked as long as matches could be identified in subsequent images. As new aggregates entered the field of view (i.e., aggregates that could not be found in previous frames), new unique identifying numbers were assigned. The algorithm continued in this fashion until the entire image time series was processed and all unique aggregates were identified. The four major steps of this algorithm are outlined below and also summarized in Fig. 6a. For ease of explanation, consider an aggregate image in one frame, called here aggregate A, being matched with a candidate aggregate image in another frame, called here aggregate B:

- 1. The algorithm first identified if aggregate B could be a potential match based on its location. More specifically, we eliminated all possible matches that would require radial motion that exceeded the maximum aggregate sinking velocity, estimated from  $w_s = 2\xi r_p^{1.17}$ , where the sinking velocity  $w_s$  was determined by the effective radius,  $r_p$ , and constant  $\xi = 1.24 \, \mathrm{cm}^{-0.17} \, \mathrm{s}^{-1}$  (Jackson 1994).
- 2. The second step required that the absolute displacement between aggregate *A* and aggregate *B* be smaller than the maximum fluid velocity inside the tank. This step reduced the number of potential matches to only those in the near vicinity to aggregate *A*.
- 3. We then evaluated the remaining candidates by calculating the minimum quadratic difference (MQD) between the sub-images of aggregate A and all possible matches. In short, the MQD quantifies the differences in pixel intensities between two images, with the minimum value obtained where two similar grayscale patterns are most aligned. Researchers widely consider MQD for PIV displacemeasurement (Merzkirch and Gui Wieneke 2015) and motion estimation based on computer vision (Yuan and Shen 2008). In our matching analysis, small MQDs meant that the images of aggregates A and B had similar shapes, sizes, and intensities and was an indication of a successful match. We considered the match to be successful if the MQD was less than two times the standard deviation of the grayscale intensities of the entire gray

image. We used this value as the reference background noise.

- a. If the MQD of all candidate matches was not small enough to meet the matching requirement, we then also evaluated the MQD ratio, MQD\_R. We defined this parameter as the ratio of the MQD to the sum of all gray pixel intensities of both aggregate sub-images squared. We considered two aggregates matched if MQD\_R < 0.1. In general, matching of smaller particles worked better using the MQD criterion, while using the MQD ratio had a better performance for larger aggregates that could deform from frame-to-frame. We have provided the details of how to calculate MQD and MQD\_R in Supporting Information S2.
- 4. A final matching step was necessary to handle the smallest observed aggregates. The images of most small aggregates were similar to one another since they were not large enough to display very unique morphologies. Thus, it was possible that multiple small aggregates close to one another could be flagged as potential matches to a small aggregate in a previous frame. Therefore, if multiple candidates for the match to aggregate *A* were still available at this step, we simply assumed that the best match was the aggregate with the smallest MQD value.

Two illumination challenges complicated this aggregate image matching procedure. First, illuminated aggregates within the light sheet could flow next to one another, briefly causing an image of a combined aggregate. Second, large unilluminated aggregates between the light sheet and the camera could briefly obscure the camera image. To prevent these events from interfering with the tracking of illuminated aggregates, we repeated the matching algorithm described above between five subsequent frames. In other words, particles would still be matched if we lost information for up to four consecutive frames. The matching procedure described above worked well (e.g., in one experiment 642,721 aggregates were identified, which reduced to 76,357 unique aggregates after the particle matching procedure).

# Breakup detection

Once the history of each aggregate was determined through the above matching algorithm, we could rely on the time-series information to detect breakup events. The basic algorithm relied on the fact that the births of two child aggregates must immediately follow the death of one parent aggregate. This case is shown schematically as Case 1 in Fig. 6b. In the early stages of a breakup event, the slight gap between two child aggregates could sometimes not be detected based on the illumination. This resulted in the breakup event taking multiple frames to be detected, with the child aggregates sometimes re-detected as a single parent aggregate for a few frames (up to 40 ms). Case 2 in Fig. 6b illustrates a valid breakup event, including binarization and

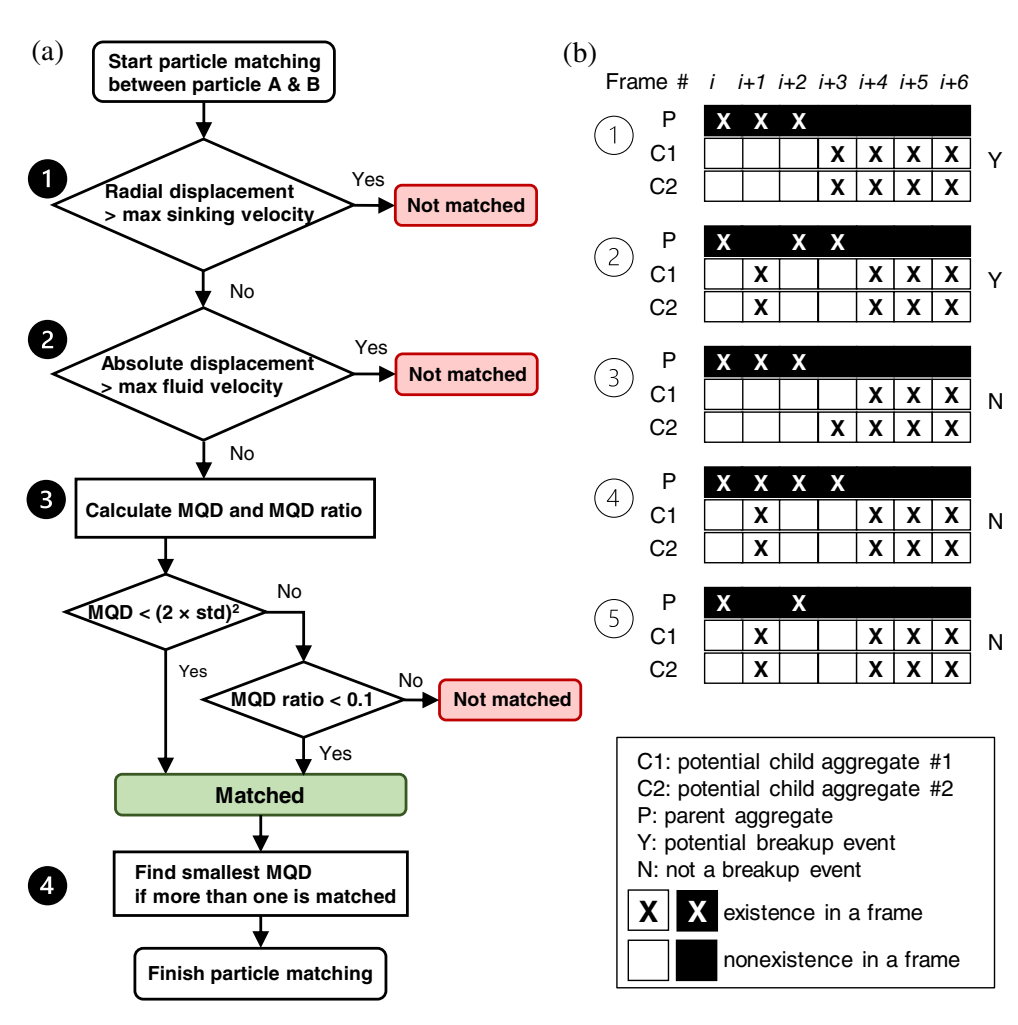


**Fig. 6.** (a) A flow chart that summarizes the four major steps of our particle matching algorithm, and (b) diagrams of the time-series correlation used to detect breakup events, showing five example cases of the detection of a parent and child aggregates in the image frames.

particle detection error. In these cases we assumed breakup occurred at the first frame where the two child aggregates were detected. In contrast, we ignored cases if two child aggregates were not born simultaneously (Case 3), if the parent and child aggregates appeared in the same frame (Case 4), or if all aggregates were missing in at least one frame (Case 5). Finally, we only analyzed breakup events where the lifespan of the parent and child particles was greater than 15 frames (> 0.12 s). This restriction conservatively eliminated short-lived aggregates from our analysis. The tracking lifespan of the aggregates analyzed in this study generally ranged from 15 to over 2000 frames, with an average of 78 frames.

Despite the rigor of the breakup detection algorithm, some aggregate images were still mistakenly identified as breakup events, for example, two aggregates passing in front of or behind one another. Thus, while the algorithm efficiently identified all possible breakup events in our aggregate populations, we also performed a manual check visually for all

breakup events to ensure accuracy. This was reasonable given the relatively rare occurrence of breakup events in the time series. We provide the detailed rubric used for the manual check in Supporting Information S3.

# Phytoplankton culture

We cultured *Odontella aurita v minima* (UTEX LB 3038) at a light intensity of  $30~\mu \text{mol m}^{-2}~\text{s}^{-1}$  on a 12 : 12 h light/dark cycle. We used filtered seawater (Gulf of Maine Seawater, Bigelow) and f/2 medium (Sigma-Aldrich) for the nutrients. The salinity was 30 ppt. During the culturing stage and experiment, we maintained the cultures at a room temperature of  $20.9^{\circ}\text{C}~(+1.2/-2.5^{\circ}\text{C})$ . We prepared the same treatment mediums using an autoclave and inoculated the culture into Erlenmeyer flasks based on their growth phase. This type of species has an average length of  $45~\mu\text{m}$  and a width of  $10~\mu\text{m}$ . We determine the equivalent spherical diameter of the culture used in our experiments to be  $15~\mu\text{m}$  from obtained micrographs.

Behavior of marine snow aggregates

#### **Assessment**

#### Stable region

Jackson (2015) introduced the concept of the stable region within a roller tank that defines the region in which particles will never have contact with the tank wall. A traditional roller tank designed for aggregation has a stable region of  $SR = (1 - w_s/\Omega R)^2$ , where  $w_s$  is the aggregate sinking velocity,  $\Omega = b/R$  is the tank rotation rate, and R is the inner radius of the tank. In contrast, defining a stable region in the disaggregation tank must consider the oscillation magnitude, a, and the oscillation frequency,  $\omega$ , in addition to the constant rotation speed, b, and the tank radius, R. Furthermore, sinking velocity depends on particle size (Jackson 1994). Hence, aggregation or fragmentation ultimately affects the stable region by influencing the aggregate settling velocities. To determine tank operating conditions that would yield a sizeable stable region for a majority of the aggregates in an experiment, we investigated the influence of these variables following the Monte Carlo computational method used by Song and Rau (2019). To simplify the problem, we assumed the instantaneous velocity of an aggregate is the vector addition of the local fluid velocity and the vertical sinking velocity, calculated according to Jackson (1994), regardless of its shape or structure. Then we randomly seeded 15,000 aggregates of the same size and sinking velocity into the tank and integrated their position over time as they were exposed to the flow velocities given by Eq. 5 in a simulated FM experiment. Two random functions distributed these monodispersed aggregates uniformly in space. The algorithm tracked each simulated aggregate until its trajectory intercepted the tank wall or the maximum simulation time was reached. Then we determined the stable region as the region bounding the starting location of all aggregates that did not impact the tank wall. We simulated up to 4h of tank operation, using a time step of 0.1 s, which more than covered the time necessary for typical fragmentation experiments.

Figure 7 displays the stable regions as a percentage of the tank volume and as a function of aggregate sinking velocity for the tank operating conditions used in Fig. 3 (a = 9 cm s<sup>-1</sup>,  $\omega = 0.5 \text{ rad s}^{-1} b = 1.5 \text{ cm s}^{-1}, R = 5 \text{ cm}, \text{ and}$  $\nu = 0.01 \text{ cm}^2 \text{ s}^{-1}$ ). The black line shows the stable region for a traditional aggregation tank (Jackson 2015). The rotating/ oscillating conditions of the disaggregation tank resulted in smaller stable regions; however, large portions of the tank were still stable for aggregates with small sinking velocity. Big aggregates with a large sinking velocity inevitably had a greater chance of contacting the tank wall. We only observed a small difference in the stable region comparing 3 min and 4 h of tank operating time, which indicates that wall collisions are not significantly influenced by the duration of operation in FM. To determine the influence of the tank operating conditions, we ran 94 simulated experiments, varying settling velocity from  $w_s = 0.006$  to 0.5 cm s<sup>-1</sup> ( $r_p = 58 \,\mu\text{m}$  to

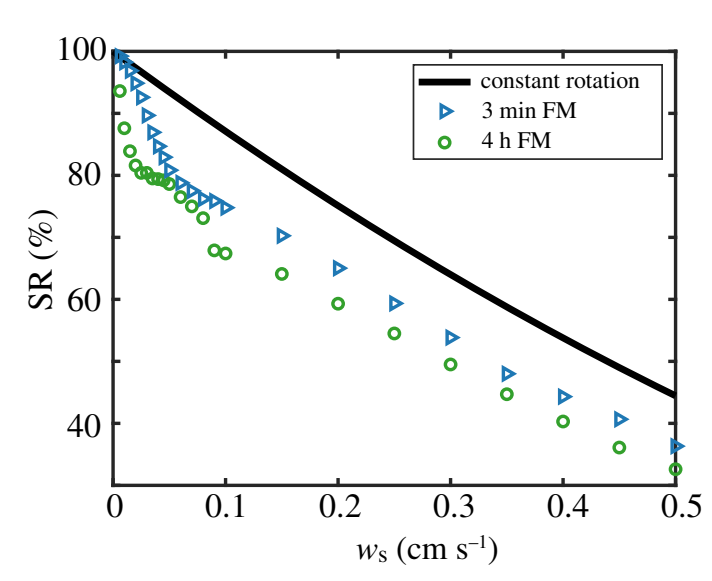


**Fig. 7.** Stable regions for varying particle sinking velocities. The black line represents the stable region for a traditional aggregation tank without time limitations (Jackson 2015). Blue and green dots are stable regions for 3 min and 4 h, respectively, of tank rotation and oscillation.

2.5 mm), oscillation magnitudes from a=0 to 15 cm s<sup>-1</sup>, constant rotation rates from b=0 to 10 cm s<sup>-1</sup>, and angular frequencies from  $\omega=0.05$  to 2 rad s<sup>-1</sup>. The variation of settling speed led to a particle Reynolds number variation from 0 to 25, which covers the range of natural marine aggregates (Alldredge and McGillivary 1991). For the tank operating conditions shown in Fig. 3 with a particle settling velocity of 5 m d<sup>-1</sup> (0.006 cm s<sup>-1</sup>), the stable region was 93.6%, which decreased as aggregate sinking velocity increased (Fig. 7). For the same base operating conditions, varying oscillation magnitude, a, showed that the stable region varied from 93.5% to 99.2%. We also did not observe significant changes in the stable region among different rotation rates, b, and different oscillation frequencies,  $\omega$ . Not surprisingly, the particle sinking velocity was the dominant factor in determining the stable region.

# Individual aggregate breakup

One of the great advantages of this experimental method is that it can capture the time-varying response of individual aggregates to shear exposure, including their morphological evolution up to and following breakup and the breakup event itself. Figure 8 provides one example fragmentation event of an aggregate with an equivalent diameter of 2.89 mm. Figure 8a–c presents the example sub-images of the parent aggregate and the two child aggregates before and after breakup. We list the experimental frame number for each image for reference, with a frame number equal to one representing the first image obtained after the tank started to oscillate. For this breakup event, we observed that the shadow created by other aggregates in the front of the tank blocked the parent aggregate at a frame number from 4588 to 4608

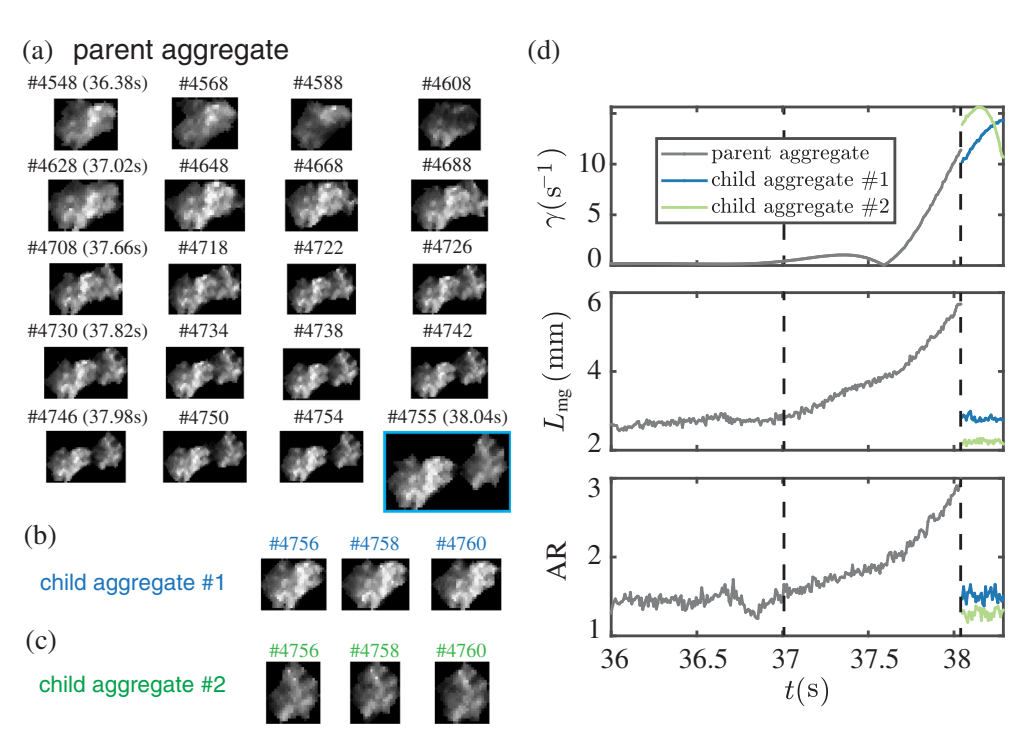


**Fig. 8.** Time series of (a) a parent aggregate elongating and breaking into the two child aggregates shown in (b) and (c). The time-resolved shear exposure of the aggregate and its resulting change in major axis length and aspect ratio are shown in (d).

(Fig. 8a). This aggregate started to elongate due to the shear exposure at a frame number of 4628 ( $t=37.02~\rm s$ ). The breakup detection determined that this parent aggregate became two separate parts at a frame number of 4755 ( $t=38.04~\rm s$ ), as shown in Fig. 8b,c.

The image processing steps allowed us to calculate morphological parameters, including equivalent diameter,  $D_{\rm eq}$ , major and minor axis length of a fitted ellipse,  $L_{\rm ma}$  and  $L_{\rm mi}$ , and aspect ratio, AR, where the aspect ratio was defined as the ratio of the major axis length to the minor axis length. Figure 8d shows the local shear rate, calculated at the aggregate centroid, the time-varying major axis length, and the time-varying aspect ratio, plotted as a function of time for the aggregate shown in Fig. 8a-c. Initially, the parent aggregate experienced low amounts of shear, which increased slightly after t = 37.02 s and then more significantly after t = 37.66 s as the aggregate settled into a near-wall region of the tank. The major axis length and aspect ratio did not increase significantly until this more considerable shear exposure, after which it elongated from  $L_{\rm ma}=2.83$  to 5.71 mm. This corresponded to a change in aspect ratio from 1.46, representing a relatively circular shape, to 2.96, representing an elongated ellipse. The aggregate broke into two smaller pieces, similar in size, at t = 38.04 s at a shear rate of 13.91 s<sup>-1</sup>.

#### Statistical fragmentation results

In addition to resolving the time-varying response of individual aggregates, the automated particle tracking algorithm

allows us to process many aggregates and investigate entire particle population statistics. We repeated the disaggregation experiment described above 25 times, starting each time with a new culture of *O. aurita*, and analyzed the resulting aggregate images. From these experiments, 180,682 aggregates were suitable (i.e., had the appropriate lighting and lifespan of greater than 15 frames) to be analyzed by our breakup detection algorithm. Fig. 9a displays the locations of the resulting 79 confirmed breakup events in the tank cross-section. Most breakup events occurred near the tank wall, where shear rates were high, as expected. It should be noted that we excluded any aggregates that were observed in contact with the wall from our analysis (*see* Supporting Information S3). We found that wall contact was rare and did not account for any confirmed breakup events in our experiments.

For comparison, we randomly selected 200 additional aggregates that did not fragment and also plotted them in Fig. 9, shown as the green crosses. To have similar local fluid shear to the fragmented aggregates, we only considered non-fragmenting aggregates located within 1 cm from the tank wall. Figure 9b,c shows the frequency histograms of aggregate aspect ratios and sizes. Disrupted aggregates had larger sizes on average and were more prone to deformation. Fragmenting aggregates tended to have higher aspect ratios than non-fragmenting aggregates, indicating that aggregate shape is an important parameter in its fragmentation, though this result was not universal. It is worth mentioning that some aggregates that had an aspect ratio of up to six did not fragment,

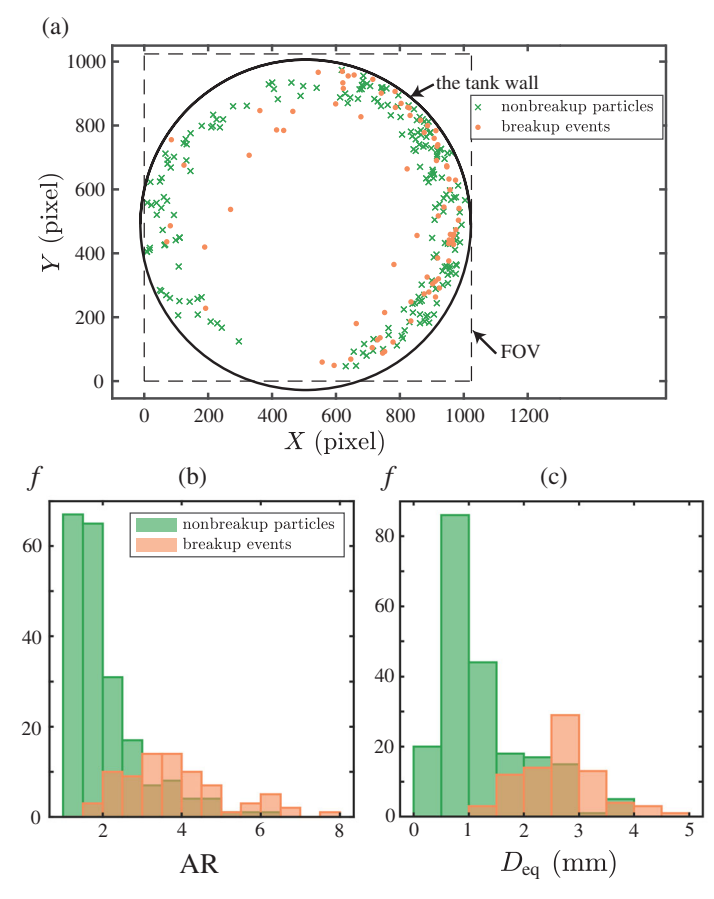


**Fig. 9.** (a) Locations of breakup events with 200 randomly selected non-fragmenting aggregates with similar shear exposure. Frequency histograms of (b) aspect ratios and (c) sizes of the fragmenting aggregates at breakup and the plotted non-fragmenting aggregates.

though most aggregates with aspect ratios above three did fragment.

In addition to analyzing individual breakup events, the images acquired from the tank can be used to build snapshots of the aggregate population and its shear exposure. Fig. 10a shows a pseudo color map of the distribution of aggregate sizes as a function of their instantaneous shear exposure from one experiment. Here, unique particles were sampled by taking all aggregates observed in every 100th image of the highspeed image sequence, which started after 3 min of operation in FM. The population was not sampled using the time-series restrictions used to detect aggregate breakup so that aggregates with lifespans of less than 15 frames could be analyzed. A total of 146,190 unique particles are displayed in Fig. 10a. Aggregate sizes ranged between 0.3 mm (our detection size limit) and 3 mm. This upper limit was based not on our optical detection method but the tank's aggregation and fragmentation conditions. The color map also shows that more particles inside the disaggregation tank were preferentially located in regions where the local shear rate was  $10^{-2}$  to  $10^{-1}$  s<sup>-1</sup>. At shear rates higher than this, the number of large aggregates

decreased, which is consistent with fragmentation. We did not observe many aggregates where the shear range was smaller than  $10^{-3}~\rm s^{-1}$  as this region was small and experienced weak fluid motion.

From the data presented in Fig. 10a, we extracted traditional particle size distributions (PSD) for aggregates exposed to similar shear rates. This is similar in concept to the PSDs presented in the literature (Spicer and Pratsinis 1996; Rau et al. 2018; Ackleson and Rau 2020). Fig. 10b shows normalized volume fractions,  $V_{\rm f}$ , of aggregates for three ranges of shear exposure, where the volume fraction of each size range,  $V_{{\rm f},D,\gamma} = \sum\limits_{i\,\in\,\{D,\gamma\}} D_{{\rm eq},i}^3/\sum\limits_{j\,\in\,\{\gamma\}} D_{{\rm eq},j}^3$ , was calculated based on the

equivalent diameter and the same shear bin. The relative volume of large particles decreased with increasing shear exposure. Meanwhile, the volume fraction of smaller particles increased. This change in the volume PSD with increasing shear is consistent with other aggregate breakup studies (Tang et al. 2000; Rau et al. 2018).

## Breakup strength of aggregated diatoms

We determined the breakup strength of one particle,  $\sigma_b$ , by assuming that it was equal to the fluid stress,  $\sigma_{\rm f}$ , experienced by that aggregate at the breakup instant, where  $\sigma_f = \mu \gamma$  was calculated at the aggregate centroid. This stress calculation is similar to that employed by Saha et al. (2016). The O. aurita aggregates in this study displayed a wide range of strengths  $(10^{-5} < \sigma_b < 10^{-1} \text{ N m}^{-2})$  even though only a fairly narrow range of aggregate diameters were sampled ( $1 < D_{eq} < 5$  mm). This variability was likely due to several reasons. First, although we cultured the O. aurita under identical conditions and started with a fresh population for each experiment, the phytoplankton in each experiment could have varied in terms of their stress level, biopolymer (i.e., transparent exopolymer particles production), and overall cohesiveness (Azetsu-Scott and Passow 2004). Second, we assumed that the fluid stress was equal to the aggregate strength at the breakup instant. In some cases where the fluid stress increases more rapidly than the aggregate could respond, it is conceivable that the fluid stress exceeded the strength of the aggregate. Finally, the strength of aggregates is known to be highly dependent on their morphology, in particular their fractal dimension (Burd and Jackson 2009). Given that aggregates from other studies, including both diatom aggregates (Alldredge et al. 1990) and aggregates of polymer beads (Bache et al. 1997; Zaccone et al. 2009; Saha et al. 2014), have shown similar variability in strength, it is most likely that the variation in our results was largely due to variations in aggregate morphology.

In Fig. 11, we compare our breakup results with the strengths of various types of aggregates reported in other studies (Alldredge et al. 1990; Bache et al. 1997; Zaccone et al. 2009; Saha et al. 2014; Song and Rau 2020b). Overall, the aggregate size was most important to determining aggregate strength. The breakup strength of diatom aggregates seemed to follow a larger general trend, where the strength followed a logarithmic decay

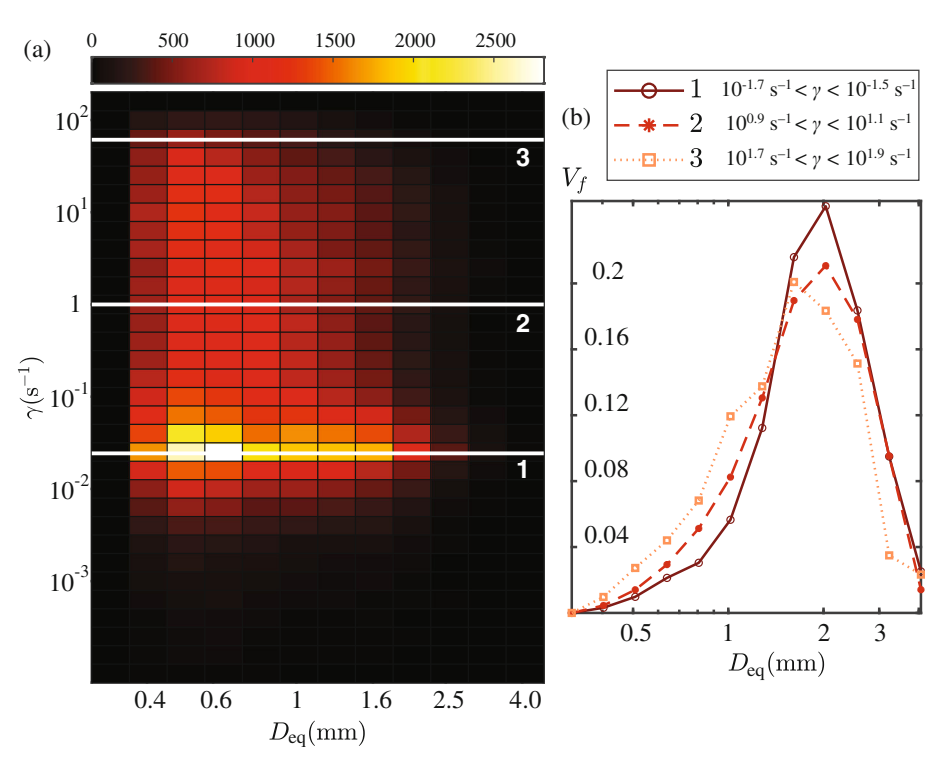


**Fig. 10.** (a) A pseudo-color plot of the number of unique particles with respect to local fluid shear and equivalent diameter and (b) normalized volume fraction vs. equivalent diameter for the three selected ranges of local fluid shear. The data plotted in (b) correspond to the numbered horizontal lines shown in (a).

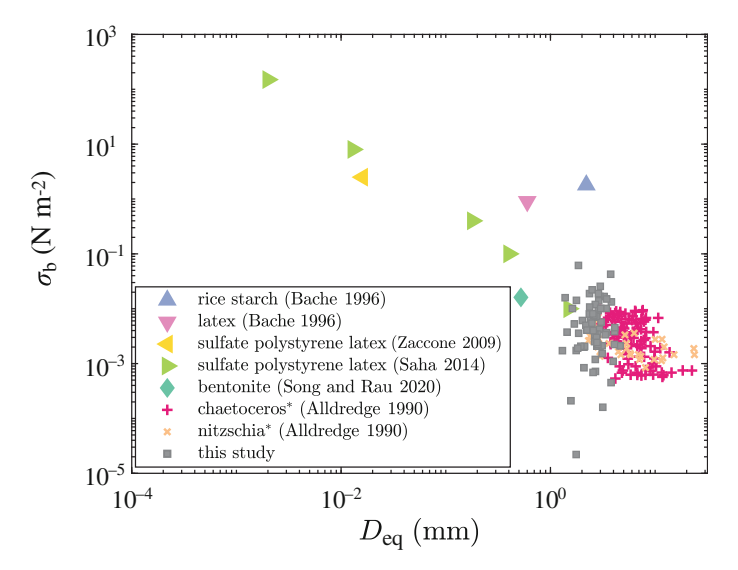


**Fig. 11.** Aggregate breakup strength as a function of aggregate size for various types of aggregates from the literature.

as aggregate size increased. The trend appeared to also apply to different types of aggregated particles materials (clays, polymer beads, and diatoms) in addition to diatom aggregates (*Chaetoceros, Nitzschia*, and *O. aurita* [this study]), which is surprising given the variability in these particle types.

## Discussion

The rotating/oscillating tank and particle tracking methods described in this study allowed for detailed resolution of aggregate fragmentation dynamics that have not yet been shown. The method allows us to uniquely study the response of aggregate morphology to shear exposure in addition to being able to resolve conditions leading to fragmentation. It further directs us to an important finding that deformation is of great importance to the fragmentation of marine aggregates. Unlike brittle materials, marine aggregates are easily deformed and can restructure in response to external forcing. This restructuring, which took the form of elongation in response to our laminar shear flow, occurred until the aggregate was too fragile to resist further elongation, resulting in fragmentation. As a result, we observed elongated morphologies prior to most fragmentation events in both our data of individual fragmentation events and the statistical results obtained. This finding emphasizes how shape and deformation factors must be considered when attempting to model the yield strength of marine aggregates.

Compared to other experimental methods, the rotating/oscillating tank is attractive in that the transition from aggregation to fragmentation mode occurs without need for manual aggregate manipulation, which can cause potential structural changes to the fragile particles. Moreover, previous fragmentation experiments have been limited to shear rates

above O(1) s<sup>-1</sup> (Alldredge et al. 1990; Goldthwait et al. 2004). Our method, in contrast, can locally resolve shear rates down to  $O(10^{-5})$  s<sup>-1</sup>. This capability has allowed us to observe the fragmentation of very fragile aggregates (e.g.,  $\sigma_{\rm b} < 10^{-4}$  N m<sup>-2</sup>, Fig. 11). The strength of these aggregates has largely not yet been quantified in the literature.

The rotating/oscillating tank does have limitations for studying marine snow fragmentation. Within natural aquatic environments, aggregates are rarely if ever made of a single diatom species. Marine aggregates typically involve more than one type of phytoplankton along with other organic detritus and possibly inorganic minerals, all of which can affect aggregate strength. Though we can employ multiple phytoplankton species and additional materials in our tank to better simulate natural marine snow particles, laboratory studies will never be able to duplicate the complexity of the ocean environment. However, this limitation is present in all laboratory investigations and is not unique to this method. One aspect of the rotating/oscillating tank that varies significantly from fragmentation in the actual marine environment is that it relies on laminar shear rather than turbulent flow, although the shear rates are similar to the more-turbulent regions of the ocean. Average turbulence dissipation rates likely underestimate the hydrodynamic forces that cause fragmentation of aggregates, as strong intermittent events can have a significant effect given that aggregate fragmentation occurs over very short timescales. While laminar shear is excellent for repeatability and for determining local shear rates around each aggregate, the use of laminar flow prevents us from studying fragmentation under the statistical variability of turbulence.

Experimentally, lighting nonuniformities and particle shadows can introduce uncertainty in the particle identification and matching process used with this method, as discussed above. Practically, this limits the particle concentration we can study as too many aggregates will obscure much of the illuminated central tank cross-section. Additionally, discontinuity caused by particle shadows limited the number of frames we could track particles so we could not obtain the entire history of shear and morphology from the very beginning of the tank oscillation. Saha et al. (2014) observed that breakage of colloidal aggregates was correlated with their exposure time to hydrodynamic forces. Future improvements that allow longer aggregate tracking could enable us to quantify time-integrated shear exposure.

We also could only resolve 2D aggregate shapes from the one-camera imaging system and could, thus, not measure their thickness along the axial direction of the tank. However, because the fluid shearing was primarily 1D in the azimuthal direction of the tank, which was captured by the imaging system, this method did capture the primary deformation length of the aggregates. Still, aggregates can have asymmetric shapes, so obtaining 3D information of their shape and volume would be desirable for future implementations of this methodology.

The particle tracking with breakup detection would also benefit from further optimization. Our current detection size limit was not sufficient to capture the morphology of the smallest aggregates in our flow. Therefore, the current analysis focused more on morphological variations and fragmentation of large aggregates. Our breakup detection algorithm also likely under-sampled fragmentation due to our conservative implementation. Based on the pseudo color plot in Fig. 10, the lack of large aggregates in the high-shear regions suggests that even moderately large aggregates readily fragmented when exposed to these shear rates. We developed this algorithm to ensure that all fragmentation events had enough morphology and time information to confidently analyze parent and child aggregates. The requirement that these aggregates be imaged for at least 15 consecutive frames ended up excluding many short-lived fragmentation events. Decreasing this time limit could potentially capture more breakup events in the aggregate population.

#### Comments and recommendations

We have described a novel rotating/oscillating tank for both aggregation and disaggregation studies. The oscillatory shear flow has shown great potential to mimic the unsteady conditions in the ocean environment to study the detailed dynamics of aggregates and other suspended materials. The magnitude of shear that the tank produces can be made comparable to that of different ocean environments by adjusting the rotating and oscillating boundary conditions. Potentially, this novel tank could be used for studying particles in very different environments, including everything from coastal sediment particles experiencing oscillatory waves above the seabed to slowly settling organic aggregates in the open ocean.

Overall, the image processing and particle matching algorithm allowed us to track individual particles as a function of time and our breakup detection method was simple and efficient. However, the required processing time was limited by the need to manually verify each breakup event. We recommend minor improvements to the experimental facility that will improve the functionality of these algorithms. Specifically, reducing the tank length to avoid the visual obscuration caused by particles in the front of the tank will increase the tracking length and improve breakup detection, so long as the shorter length does not invalidate the 2D flow assumption along the central plane. This modification will also allow the imaging system to track a greater percentage of the particles in the tank at one time and, in conjunction with refining our breakup detection thresholds, will facilitate the capture of a greater number of breakup events in a given aggregate population. We also plan to employ a new high-speed imaging system with greater imaging magnification, which will decrease the aggregate size detection limit. It should be noted that the presented method can be used to capture long-term population changes as well as the short-duration fragmentation events presented above.

Though the memory capacity of the imaging system determines the overall data collection length, lower-speed imaging systems with continuous recording or the acquisition of population snapshots in time can be used to measure the evolution of population size spectra for much longer than the 175 s recordings acquired in these experiments.

In the future, we will continue exploring more biophysics with this novel method. In particular, we hope to investigate the role of shear history in the breakup of aggregates in addition to the influence of aggregate makeup and structure on overall aggregate strength. In addition to allowing us to study fragmentation, this method also provides a means to acquire large datasets of aggregate deformation in response to shear. The strain characteristics of these aggregates could potentially be used to extract additional mechanical properties of the aggregates and their cohesive component particles.

#### Data availability statement

The authors confirm that the data supporting the findings of this study are available within the article.

#### References

- Ackleson, S. G., and M. J. Rau. 2020. A method to measure marine particle aggregate disruption in situ. Limnol Oceanogr Methods, **18**: 644-655. doi:10.1002/lom3.10391
- Alldredge, A. L., and C. Gotschalk. 1988. In situ settling behavior of marine snow1. Limnol. Oceanogr. **33**: 339–351. doi:10.4319/lo.1988.33.3.0339
- Alldredge, A. L., and M. W. Silver. 1988. Characteristics, dynamics and significance of marine snow. Prog. Oceanogr. **20**: 41–82. doi:10.1016/0079-6611(88)90053-5
- Alldredge, A. L., T. C. Granata, C. C. Gotschalk, and T. D. Dickey. 1990. The physical strength of marine snow and its implications for particle disaggregation in the ocean. Limnol. Oceanogr. **35**: 1415–1428. doi:10.4319/lo.1990.35.7.1415
- Alldredge, A. L., and P. McGillivary. 1991. The attachment probabilities of marine snow and their implications for particle coagulation in the ocean. Deep Sea Res. Part A Oceanogr. Res. Pap. **38**: 431–443. doi:10.1016/0198-0149(91)90045-H
- Aumont, O., C. Ethé, A. Tagliabue, L. Bopp, and M. Gehlen. 2015. PISCES-v2: An ocean biogeochemical model for carbon and ecosystem studies. Geosci. Model Dev. **8**: 2465–2513. doi:10.5194/gmd-8-2465-2015
- Azetsu-Scott, K., and U. Passow. 2004. Ascending marine particles: Significance of transparent exopolymer particles (TEP) in the upper ocean. Limnol. Oceanogr. **49**: 741–748. doi: 10.4319/lo.2004.49.3.0741
- Bache, D. H., C. Johnson, J. F. McGilligan, and E. Rasool. 1997. A conceptual view of floc structure in the sweep floc domain. Water Sci. Technol. **36**: 49–56. doi:10.1016/S0273-1223(97)00418-6
- Berger, W. H., K. Fischer, C. Lai, and G. Wu 1988. Ocean carbon flux: Global maps of primary production and export

- production, p. 131–176. *In* C. R. Agegian [ed.], Biogeochemical cycling and fluxes between the deep euphotic zone and other oceanic realms. National Undersea Research Program research report 88–1. NOAA.
- Briggs, N., G. Dall'Olmo, and H. Claustre. 2020. Major role of particle fragmentation in regulating biological sequestration of CO<sub>2</sub> by the oceans. Science **367**: 791–793. doi:10. 1126/science.aay1790
- Burd, A. B., and G. A. Jackson. 2009. Particle aggregation. Ann. Rev. Mar. Sci. **1**: 65–90. doi:10.1146/annurev.marine. 010908.163904
- Cael, B. B., E. L. Cavan, and G. L. Britten. 2021. Reconciling the size-dependence of marine particle sinking speed. Geophys. Res. Lett. **48**: e2020GL091771. doi:10.1029/2020GL091771
- Collins, J. R., B. R. Edwards, K. Thamatrakoln, J. E. Ossolinski, G. R. Ditullio, K. D. Bidle, S. C. Doney, and B. A. S. Van Mooy. 2015. The multiple fates of sinking particles in the North Atlantic Ocean. Global Biogeochem. Cycles **29**: 1471–1494. doi:10.1002/2014GB005037
- Dillon, T. M., and D. R. Caldwell. 1980. The Batchelor spectrum and dissipation in the upper ocean. J. Geophys. Res. **85**: 1910. doi:10.1029/JC085iC04p01910
- Fowler, S. W., and G. A. Knauer. 1986. Role of large particles in the transport of elements and organic compounds through the oceanic water column. Prog. Oceanogr. **16**: 147–194. doi:10.1016/0079-6611(86)90032-7
- Franks, P. J. S., B. G. Inman, J. A. MacKinnon, M. H. Alford, and A. F. Waterhouse. 2022. Oceanic turbulence from a planktonic perspective. Limnol. Oceanogr. **67**: 348–363. doi:10.1002/lno.11996
- Fuchs, H. L., L. S. Mullineaux, and A. R. Solow. 2004. Sinking behavior of gastropod larvae ( *Ilyanassa obsoleta*) in turbulence. Limnol. Oceanogr. **49**: 1937–1948. doi:10.4319/lo. 2004.49.6.1937
- George, R., R. E. Flick, and R. T. Guza. 1994. Observations of turbulence in the surf zone. J. Geophys. Res. **99**: 801. doi: 10.1029/93JC02717
- Goldthwait, S., J. Yen, J. Brown, and A. Alldredge. 2004. Quantification of marine snow fragmentation by swimming euphausiids. Limnol. Oceanogr. **49**: 940–952. doi:10.4319/lo.2004.49.4.0940
- Gross, T. F., and A. R. M. Nowell. 1985. Spectral scaling in a tidal boundary layer. J. Phys. Oceanogr. **15**: 496–508. doi: 10.1175/1520-0485(1985)015<0496:SSIATB>2.0.CO;2
- Jackson, G. A. 1994. Particle trajectories in a rotating cylinder: Implications for aggregation incubations. Deep. Res. Part I 41: 429–437. doi:10.1016/0967-0637(94)90089-2
- Jackson, G. A. 2015. Coagulation in a rotating cylinder. Limnol. Oceanogr. Methods 13: 194–201. doi:10.1002/ lom3.10018
- Johnson, C. P., X. Li, and B. E. Logan. 1996. Settling velocities of fractal aggregates. Environ. Sci. Technol. **30**: 1911–1918. doi:10.1021/es950604g

- Kiørboe, T. 2001. Formation and fate of marine snow: Small-scale processes with large-scale implications. Sci. Mar. **65**: 57–71. doi:10.3989/scimar.2001.65s257
- Kwon, E. Y., F. Primeau, and J. L. Sarmiento. 2009. The impact of remineralization depth on the air–sea carbon balance. Nat. Geosci. **2**: 630–635. doi:10.1038/ngeo612
- Mendez, M. A., M. Raiola, A. Masullo, S. Discetti, A. Ianiro, R. Theunissen, and J.-M. Buchlin. 2017. POD-based background removal for particle image velocimetry. Exp. Therm. Fluid Sci. **80**: 181–192. doi:10.1016/j.expthermflusci.2016.08.021
- Merzkirch, W., and L. Gui. 2000. A comparative study of the MQD method and several correlation-based PIV evaluation algorithms. Exp. Fluids **28**: 36–44. doi:10.1007/s003480050005
- Middelburg, J. J. 2011. Chemoautotrophy in the ocean. Geophys. Res. Lett. **38**: L24604. doi:10.1029/2011GL049725
- Muller-Karger, F. E., R. Varela, R. Thunell, R. Luerssen, C. Hu, and J. J. Walsh. 2005. The importance of continental margins in the global carbon cycle. Geophys. Res. Lett. **32**: L01602. doi:10.1029/2004GL021346
- Rau, M. J., S. G. Ackleson, and G. B. Smith. 2018. Effects of turbulent aggregation on clay floc breakup and implications for the oceanic environment. PLoS One **13**: e0207809. doi:10.1371/journal.pone.0207809
- Saha, D., M. Soos, B. Lüthi, M. Holzner, A. Liberzon, M. U. Babler, and W. Kinzelbach. 2014. Experimental characterization of breakage rate of colloidal aggregates in axisymmetric extensional flow. Langmuir 30: 14385–14395. doi: 10.1021/la502686b
- Saha, D., M. U. Babler, M. Holzner, M. Soos, B. Lüthi, A. Liberzon, and W. Kinzelbach. 2016. Breakup of finite-size colloidal aggregates in turbulent flow investigated by three-dimensional (3D) particle tracking velocimetry. Langmuir 32: 55–65. doi:10.1021/acs.langmuir.5b03804
- Shanks, A. L., and E. W. Edmondson. 1989. Laboratory-made artificial marine snow: A biological model of the real thing. Mar. Biol. **101**: 463–470. doi:10.1007/BF00541648
- Song, Y., and M. J. Rau. 2019. Characterization of aggregate disruption using organic marine particles and particle tracking measurements in rotating/oscillating aggregation tanks. Volume 5: Multiphase flow. American Society of Mechanical Engineers, p. 1–7.
- Song, Y., and M. J. Rau. 2020a. Viscous fluid flow inside an oscillating cylinder and its extension to Stokes' second problem. Phys. Fluids **32**: 043601. doi:10.1063/1.5144415
- Song, Y., and M. J. Rau. 2020b. Disruption behavior of aggregates in a rotating/oscillating cylindrical tank and implications for particle transport in the ocean. Volume 2: Fluid

- mechanics; multiphase flows. American Society of Mechanical Engineers.
- Spicer, P.T. and S. E. Pratsinis. 1996. Coagulation and fragmentation: Universal steady-state particle-size distribution. AIChE J, **42**: 1612-1620. doi:10.1002/aic.690420612
- Tang, S., J. M. Preece, C. M. McFarlane, and Z. Zhang. 2000. Fractal morphology and breakage of DLCA and RLCA aggregates. J. Colloid Interface Sci. 221: 114–123. doi:10.1006/jcis.1999.6565
- Torza, S., R. G. Cox, and S. G. Mason. 1972. Particle motions in sheared suspensions XXVII. Transient and steady deformation and burst of liquid drops. J. Colloid Interface Sci. **38**: 395–411. doi:10.1016/0021-9797(72)90255-X
- Wieneke, B. 2015. PIV uncertainty quantification from correlation statistics. Meas. Sci. Technol. **26**: 074002. doi:10.1088/0957-0233/26/7/074002
- Williams, A., J. J. M. Janssen, and A. Prins. 1997. Behaviour of droplets in simple shear flow in the presence of a protein emulsifier. Colloids Surf. Physicochem. Eng. Asp. **125**: 189–200. doi:10.1016/S0927-7757(96)03972-6
- Yuan, X., and X. Shen. 2008. Block matching algorithm based on particle swarm optimization for motion estimation. *In* 2008 International Conference on Embedded Software and Systems. IEEE.
- Zaccone, A., M. Soos, M. Lattuada, H. Wu, M. U. Bäbler, and M. Morbidelli. 2009. Breakup of dense colloidal aggregates under hydrodynamic stresses. Phys. Rev. E 79: 061401. doi: 10.1103/PhysRevE.79.061401
- Ziervogel K, Sweet J, Bretherton L, Quigg A, and Passow U. 2020. Fragmentation of marine snow and marine oil snow due to small-scale turbulence. Ocean Sciences Meeting 2020.

#### Acknowledgments

The authors gratefully acknowledge support for this research through NSF grant OCE-1948283. We are particularly thankful for the expertise Dr. Adrian Burd has shared in our past and continuing discussion of this work. We also wish to thank Dr. Margaret Byron, Dr. Robert Kunz, and Dr. Raymond Najjar, for their helpful discussions and constructive recommendations.

#### Conflict of interest

None declared.

Submitted 12 February 2022 Revised 04 August 2022 Accepted 08 August 2022

Associate editor: Scott Ensign